Chemical Science

ROYAL SOCIETY OF CHEMISTRY

EDGE ARTICLE

View Article Online
View Journal | View Issue

Check for updates

Cite this: *Chem. Sci.*, 2023, **14**, 2528

All publication charges for this article have been paid for by the Royal Society of Chemistry

Received 31st December 2022
Accepted 9th February 2023

DOI: 10.1039/d2sc07121e

rsc.li/chemical-science

Bond modulation of $MoSe_{2+x}$ driving combined intercalation and conversion reactions for high-performance K cathodes†

Ting Lei,‡[a] Mingyuan Gu,‡[a] Hongwei Fu,[a] Jue Wang,[b] Longlu Wang,[c] Jiang Zhou,[d] Huan Liu[e] and Bingan Lu *[a]

The urgent demand for large-scale global energy storage systems and portable electronic devices is driving the need for considerable energy density and stable batteries. Here, Se atoms are introduced between $MoSe_2$ layers (denoted as $MoSe_{2+x}$) by bond modulation to produce a high-performance cathode for potassium-ion batteries. The introduced Se atoms form covalent Se–Se bonds with the Se in $MoSe_2$, and the advantages of bond modulation are as follows: (i) the interlayer spacing is enlarged which increases the storage space of K^+; (ii) the system possesses a dual reaction mechanism, and the introduced Se can provide an additional conversion reaction when discharged to 0.5 V, which improves the capacity further; (iii) the Se atoms confined between $MoSe_2$ layers do not give rise to the shuttle effect. $MoSe_{2+x}$ is compounded with rGO ($MoSe_{2+x}$-rGO) as a cathode for potassium-ion batteries and displays an ultrahigh capacity (235 mA h g^{-1} at 100 mA g^{-1}), a long cycle life (300 cycles at 100 mA g^{-1}) and an extraordinary rate performance (135 mA h g^{-1} at 1000 mA g^{-1} and 89 mA h g^{-1} at 2000 mA g^{-1}). Pairing the $MoSe_{2+x}$-rGO cathode with graphite, the full cell delivers considerable energy density compared to other K cathode materials. The $MoSe_{2+x}$-rGO cathode also exhibits excellent electrochemical performance for lithium-ion batteries. This study on bond modulation driving combined intercalation and conversion reactions offers new insights into the design of high-performance K cathodes.

Introduction

Two-dimensional (2D) transition metal dichalcogenides (TMDCs) are widely applied in energy storage.[1,2] Molybdenum diselenide ($MoSe_2$), as a representative TMDC, is a promising electrode material for alkali metal ion batteries owing to its layered structure, chemical stability, high reversible capacity, and appropriate working potential.[3–6] Moreover, $MoSe_2$ has a higher conductivity (1×10^{-3} S m^{-1}, Se gives rise to the metallic nature) and a larger interlayer spacing ($\approx$6.4 Å) than the corresponding sulfides, suggesting that $MoSe_2$ can better accommodate the alkali metal ions.[6,7] However, as a 2D material, the pristine $MoSe_2$ tends to stack and aggregate, which has a detrimental impact on the cycling performance.[8,9] More seriously, the pristine $MoSe_2$ undergoes a huge volume expansion during electrochemical cycling, leading to structural collapse and poor electrochemical performance.[10,11] As a result, the pristine $MoSe_2$, despite its many advantages, has difficulty in realizing its full potential. To solve the above problems, many sophisticated molecular engineering strategies have been used to modify $MoSe_2$ in recent years.[6,12] These molecular engineering strategies can be broadly classified into five categories: interfacial engineering,[13] structural engineering,[14] doping engineering,[15] phase engineering[16] and defect engineering.[17] However, the improvement of performance of $MoSe_2$ by these traditional modification methods is very highly limited by its theoretical capacity within a specific voltage range. Therefore, there is an urgent need to find a method to modulate $MoSe_2$ itself to improve the upper limit of its electrochemical performance.

According to research on the reaction mechanism of $MoSe_2$, only a single intercalation reaction occurs for $MoSe_2$ when discharged to 0.5 V.[15,18,19] And the reaction mechanism of cathode materials in potassium-ion batteries (PIBs) is mainly intercalation.[20] However, intercalation-type electrode materials

---

[a] School of Physics and Electronics, Hunan University, Changsha 410082, P. R. China. E-mail: luba2012@hnu.edu.cn

[b] College of Chemistry and Chemical Engineering, Central South University, Changsha 410083, P. R. China

[c] Jiangsu Province Engineering Research Center for Fabrication and Application of Special Optical Fiber Materials and Devices, Nanjing University of Posts & Telecommunications, Nanjing 210003, P. R. China

[d] School of Materials Science and Engineering, Central South University, Changsha 410083, P. R. China

[e] Hunan Provincial Key Lab of Advanced Materials for New Energy Storage and Conversion, Hunan University of Science and Technology, Xiangtan 411201, P. R. China

† Electronic supplementary information (ESI) available. See DOI: https://doi.org/10.1039/d2sc07121e

‡ These authors contributed equally.

are known to have some non-negligible defects, such as low discharge capacity and slow diffusion kinetics, although they exhibit excellent stability.[21,22] In contrast, high capacity can be achieved in conversion-type electrode materials. But the conversion reaction usually suffers from large volume change and the shuttle effect, which is unfavorable for electrochemical performance.[21,23–25] Thus far, it is still a huge challenge to realize high capacity and stable cycling in cathodes. Consequently, developing cathode materials with a combinational reaction mechanism to integrate the advantages of each component should be an effective path to resolving the above problems. The dual reaction mechanism with intercalation and conversion reactions has been recently reported for lithium-ion cathode materials.[26] However, there is no relevant report on potassium-ion cathodes.

Here, Se atoms are introduced between $MoSe_2$ layers (denoted as $MoSe_{2+x}$) by a bond modulation strategy to raise the capacity ceiling and improve the stability of $MoSe_2$. The introduced Se atoms form covalent Se–Se bonds with the Se in $MoSe_2$, and collaborate with $MoSe_2$ to modulate the performance of $MoSe_{2+x}$, bringing the following benefits: (i) the enlarged interlayer spacing due to the bond modulation can accelerate K^+ transport, improving the rate performance; (ii) the Se atoms between $MoSe_2$ layers undergo conversion reaction when discharged to 0.5 V, which provides additional capacity; (iii) the introduced Se atoms are independent of each other, thereby displaying no shuttle effect during cycling, which enhances the cycling stability.[24] Besides, we verified, by density functional theory (DFT) calculations, that $MoSe_{2+x}$ with a larger interlayer spacing could accommodate more K^+ than $MoSe_2$. To further enhance the cycling stability, $MoSe_{2+x}$ was compounded with rGO (denoted as $MoSe_{2+x}$-rGO). As a result, $MoSe_{2+x}$-rGO as a cathode for PIBs displays an ultrahigh capacity (235 mA h g^{-1} at 100 mA g^{-1}), a long cycle life (300 cycles at 100 mA g^{-1}) and an extraordinary rate performance (135 mA h g^{-1} at 1000 mA g^{-1} and 89 mA h g^{-1} at 2000 mA g^{-1}). Matching the $MoSe_{2+x}$-rGO cathode with graphite, the full cell delivers considerable energy density compared to other K cathode materials.[20,27] The $MoSe_{2+x}$-rGO cathode also exhibits excellent electrochemical performance for lithium-ion batteries (LIBs).

Results and discussion

Fig. 1a illustrates our bond modulation strategy by introducing selenium atoms randomly between $MoSe_2$ layers to improve the upper limit of $MoSe_2$'s electrochemical performance. $MoSe_{2+x}$ has a sandwich structure, where the anchored Se atoms between the $MoSe_2$ layers and $MoSe_2$ collaborate with each other. First, the interlayer spacing of $MoSe_2$ is enlarged due to the modulation of Se–Se bonds, which allows more K^+ to be embedded into the interlayer; second, this special structure yields a dual reaction mechanism for $MoSe_{2+x}$. The interlayer Se atoms within $MoSe_{2+x}$ provide an additional conversion reaction, while $MoSe_2$ displays a single intercalation reaction in the same voltage window (0.5–3 V) (Fig. 1b and c).[15,18] In addition, the introduced Se atoms are anchored in the interlayer with no appearance of long-chain molecular Se, thereby avoiding the shuttle effect.[24] Through this bond modulation strategy, the upper performance limit of $MoSe_2$ is greatly improved, and a high-performance cathode is achieved.

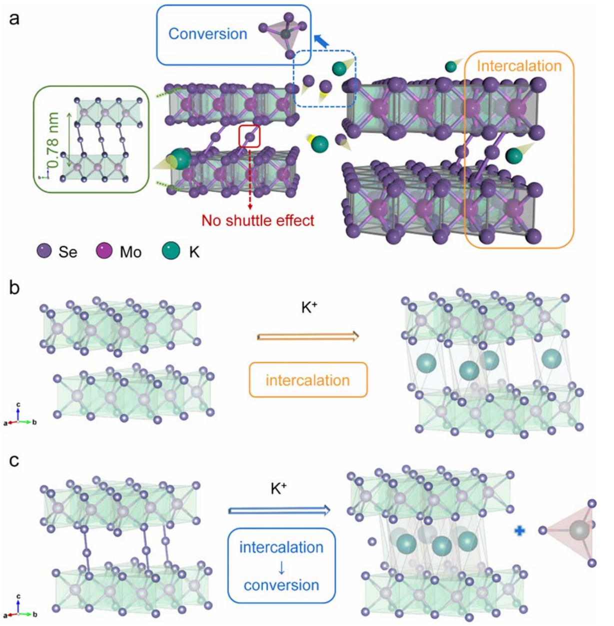

Fig. 1 (a) Schematic illustration of the modulation of Se–Se bonds. (b and c) Crystal structure and mechanism of $MoSe_2$ and $MoSe_{2+x}$, respectively. Purple atoms represent selenium, pink atoms represent molybdenum, and green atoms represent potassium.

$MoSe_{2+x}$ and the $MoSe_{2+x}$-rGO composite were synthesized by a one-step hydrothermal method (Fig. S1†). The control electrode material $MoSe_2$-rGO was obtained by annealing $MoSe_{2+x}$-rGO. The energy-dispersive X-ray spectroscopy (EDS) elemental analysis results (Fig. S2†) revealed that the value of x in $MoSe_{2+x}$-rGO was around 0.2. The scanning electron microscopy (SEM) image of $MoSe_2$-rGO revealed a lumpy particle morphology with a diameter larger than 150 nm (Fig. 2a). The SEM image of $MoSe_{2+x}$-rGO showed a coral-like structure composed of a large number of nanosheets (Fig. 2b). These characteristics of $MoSe_{2+x}$-rGO were also displayed in the transmission electron microscope (TEM) image (Fig. S3†). The EDS mapping images of $MoSe_{2+x}$-rGO showed that Mo, Se and C elements were evenly distributed (Fig. S4†). The crystal structure of $MoSe_2$ is exhibited in Fig. 1b, and the Mo atoms (pink) stayed at the center of the triangular prism, with Se atoms (purple) at the vertices forming an Se–Mo–Se triangular prism unit cell. The crystal structure of $MoSe_{2+x}$ is displayed in Fig. 1c. The excess Se atoms (except for the Se atoms in $MoSe_2$) were randomly distributed in the triangular prism sites in the van der Waals gap. The modulation of Se–Se bonds has been proved to increase the electronic conductivity.[28] The high-resolution transmission electron microscopy (HRTEM) images of $MoSe_2$-rGO and $MoSe_{2+x}$-rGO exhibited distinct lattice fringes (Fig. 2c and d). The interplanar spacing of $MoSe_2$ was measured to be 0.65 nm, which matched well with the (002) lattice planes of the 2H-$MoSe_2$ phase (JCPDS no. 29-0914). And the interplanar spacing of $MoSe_{2+x}$ was expanded to 0.78 nm by the modulation

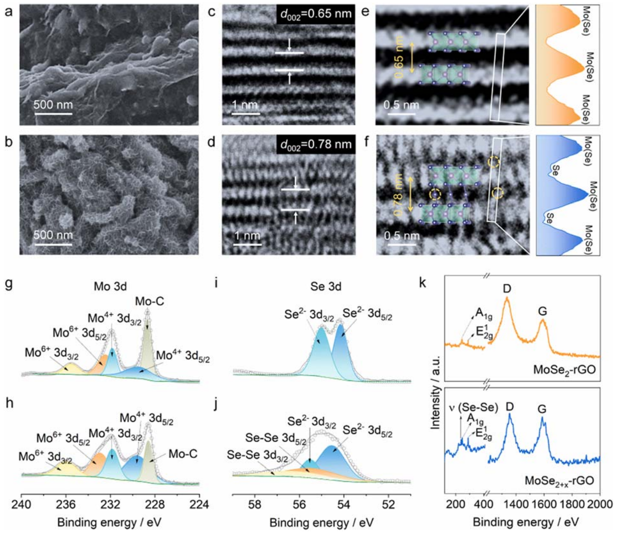

Fig. 2 Morphology and structure characterization. SEM images of (a) $MoSe_2$-rGO and (b) $MoSe_{2+x}$-rGO. HRTEM images of (c) $MoSe_2$-rGO and (d) $MoSe_{2+x}$-rGO. Atomic images of (e) $MoSe_2$-rGO and (f) $MoSe_{2+x}$-rGO; the line scan profiles along the corresponding rectangles are shown on the right. XPS spectra of (g and i) $MoSe_2$-rGO and (h and j) $MoSe_{2+x}$-rGO. (k) Raman spectra of $MoSe_2$-rGO and $MoSe_{2+x}$-rGO.

of Se–Se bonds. The atomic images of $MoSe_2$-rGO and $MoSe_{2+x}$-rGO are shown in Fig. 2e and f, where there were grains projected along the [002] zone axis, with the large bright area representing $MoSe_2$. The difference was that the atomic image of $MoSe_{2+x}$-rGO displayed excess Se atoms between $MoSe_2$ layers (some positions did not). The introduction of Se atoms was also proven by line-scan intensity profiles (Fig. 2e and f).[29] The X-ray diffraction (XRD) pattern of $MoSe_2$-rGO is displayed in Fig. S5,† illustrating a good crystallinity with peaks well indexed to 2H-$MoSe_2$ and a sharp peak at 26° attributed to rGO.[30,31] The broadened diffraction peaks (especially the (002) plane) of pure $MoSe_{2+x}$ and $MoSe_{2+x}$-rGO revealed that $MoSe_{2+x}$ had a structure of few layers and relatively low crystallinity (Fig. 2d and S6†).[32,33] It is noteworthy that the (002) peak of $MoSe_{2+x}$ and $MoSe_{2+x}$-rGO shifted to a lower angle position, indicating that the interplanar spacing along the [002] axis was enlarged. The selected area electron diffraction (SAED) patterns of $MoSe_2$-rGO and $MoSe_{2+x}$-rGO both gave distinct crystal diffraction rings (Fig. S7†).

The chemical compositions and valence states of the $MoSe_2$-rGO and $MoSe_{2+x}$-rGO composites were analyzed by X-ray photoelectron spectroscopy (XPS). The investigated spectra of $MoSe_2$-rGO and $MoSe_{2+x}$-rGO both showed four main elements: Mo, Se, C and O (Fig. S8 and S9†), which was consistent with the EDS results. In the high-resolution Mo 3d spectra (Fig. 2g and h), both $MoSe_{2+x}$-rGO and $MoSe_2$-rGO displayed one doublet at 229.5 and 231.8 eV, which was assigned to the Mo $3d_{5/2}$ and $3d_{3/2}$ characteristic peaks of Mo^{4+}, while the other doublet at 232.9 and 236.0 eV was due to the presence of Mo^{6+}. Additionally, the Mo 3d spectra of $MoSe_2$-rGO and $MoSe_{2+x}$-rGO both showed a peak at 228.6 eV, which was ascribed to the Mo–C bond, verifying that both $MoSe_2$ and $MoSe_{2+x}$ were successfully compounded with rGO.[30] The high resolution Se 3d spectra of $MoSe_2$-rGO and $MoSe_{2+x}$-rGO in Fig. 2i and j both displayed a doublet at approximately 54.6 and 55.5 eV, which was indexed to the Se $3d_{5/2}$ and $3d_{3/2}$ characteristic peaks of monoselenide (Se^{2-}). But the Se 3d spectrum of $MoSe_{2+x}$-rGO showed another doublet at 55.5 and 56.2 eV, which was attributed to the Se $3d_{5/2}$ and $3d_{3/2}$ characteristic peaks of homopolar Se–Se bonds.[34,35] As illustrated in Fig. 2k, the Raman spectrum of $MoSe_{2+x}$ had an out-of-plane Mo–Se phonon mode (A_{1g}) located at 244 cm^{-1} and an in-plane Mo–Se phonon mode ($E^1{}_{2g}$), which were the characteristic peaks of $MoSe_2$.[18,30,36] In addition, it also showed a sharp peak at 237 cm^{-1} arising from the intrachain stretching vibration mode of homopolar Se–Se bonds.[24,37] As shown in Fig. S10a,† the nitrogen adsorption–desorption isotherms of $MoSe_2$-rGO and $MoSe_{2+x}$-rGO both exhibited a distinct hysteresis loop, which belonged to type IV, revealing the existence of mesoporous structures in the materials. The measured specific surface area of $MoSe_{2+x}$-rGO was 21.931 m^2 g^{-1} with a main pore diameter of 6.408 nm (Fig. S10b†). By comparison, the $MoSe_2$-rGO had a smaller specific surface area (14.932 m^2 g^{-1}) and a smaller main pore diameter (2.753 nm). In addition, to achieve accurate loading of $MoSe_{2+x}$ in $MoSe_{2+x}$-rGO, thermogravimetric analyses (TGA) of pure $MoSe_{2+x}$ and $MoSe_{2+x}$-rGO were performed (Fig. S11†). By comparing the results of their TGA data, the content of $MoSe_{2+x}$ in the $MoSe_{2+x}$-rGO composite was found to be about 92.53 wt%.

The electrochemical performance of the $MoSe_{2+x}$-rGO was investigated as the cathode for PIBs. Fig. 3a displays the first three cyclic voltammogram (CV) curves in the voltage window of 0.5–3.0 V *versus* K^+/K at a scan rate of 0.1 mV s^{-1}. There were two cathodic peaks at 1.52 and 0.82 V observed because of K^+ uptake in the initial cycle that disappeared in the subsequent cycles,

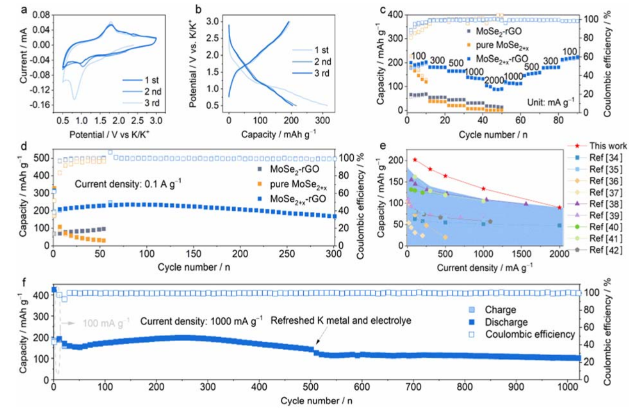

Fig. 3 Electrochemical performance of $MoSe_{2+x}$-rGO for potassium-ion storage. (a) CV profiles of $MoSe_{2+x}$-rGO at the 1st, 2nd and 3rd cycles. (b) Discharge/charge curves of $MoSe_{2+x}$-rGO at the 1st, 2nd and 3rd cycles. (c) Rate performance of pure $MoSe_{2+x}$, $MoSe_{2+x}$-rGO and $MoSe_2$-rGO at various current densities. (d) Cycling performance of $MoSe_{2+x}$-rGO, pure $MoSe_{2+x}$ and $MoSe_2$-rGO at 100 mA g^{-1}. (e) Comparison of the capacity of $MoSe_{2+x}$-rGO with those of other cathodes at different current densities for PIBs (blue represents Prussian blue analogues/cyanoferrates, orange represents polyanionic compounds, purple represents metal oxides, green represents organic materials, and grey represents metal organic frameworks). (f) Cycling performance of $MoSe_{2+x}$-rGO at 1000 mA g^{-1}.

which were attributed to the irreversible side reactions and the formation of a solid electrolyte interphase (SEI) on the electrode surface.[15,38] In terms of the anodic scan, the strong peak at 1.79 V could be related to the process of K^+ release.[15] With the continuation of sweeping, two new cathodic peaks appeared at 2.15 and 0.98 V, indicating the intercalation of K^+ into $MoSe_{2+x}$. The almost overlapping anodic and cathodic peaks in the subsequent cycles were an indication of the highly reversible redox behaviors of this electrode. The voltage plateaus of the charge/discharge profiles (Fig. 3b) were consistent with the CV curves. The $MoSe_{2+x}$-rGO showed a superior rate performance (Fig. 3c and S12†), retaining capacities of 203, 182, 165, 135 and 89 mA h g^{-1} at current densities of 100, 300, 500, 1000 and 2000 mA g^{-1}. When the current density returned to 100 mA g^{-1}, the discharge capacity could still return to 210 mA h g^{-1}, which was comparable with the initial discharge capacity. However, the rate performance of $MoSe_2$-rGO and pure $MoSe_{2+x}$ was much inferior to that of $MoSe_{2+x}$-rGO because of the absence of modulation of Se–Se bonds and the combination with rGO, respectively. The high capacity of $MoSe_{2+x}$-rGO dominated those of various other cathodes for PIBs (Fig. 3e).[39–47] The long-duration cycling performance of $MoSe_{2+x}$-rGO, $MoSe_2$-rGO and pure $MoSe_{2+x}$ at 100 mA g^{-1} is shown in Fig. 3d. Impressively, $MoSe_{2+x}$-rGO exhibited a high initial charge capacity of 195 mA h g^{-1}, and a capacity of 168 mA h g^{-1} could still be achieved after 300 cycles. The coulombic efficiency (CE) was above 99.5% on average. Compared with $MoSe_2$-rGO, the $MoSe_{2+x}$-rGO electrode had an overwhelming advantage in capacity. Even though the pure $MoSe_{2+x}$ had a comparable initial capacity to $MoSe_{2+x}$-rGO, its capacity decayed quickly without the stability effect of rGO. The outstanding cycle life (nearly 1300 h) and the impressive rate performance of $MoSe_{2+x}$-rGO surpassed those of the reported $MoSe_2$-based composite electrodes in PIBs (Fig. S13 and Table S1†).[30,48–54] The cycling performance of $MoSe_{2+x}$-rGO at a high current density of 1000 mA g^{-1} is presented in Fig. 3f. $MoSe_{2+x}$-rGO retained a high specific capacity of 101 mA h g^{-1} over 1020 cycles (with pre-cycling at 100 mA g^{-1} for 20 cycles). Moreover, the CE was maintained above 99.7% on average.

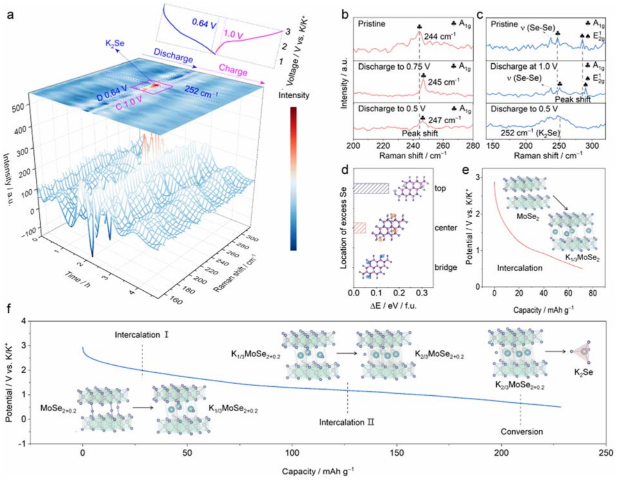

Fig. 4 Structural evolution of $MoSe_{2+x}$-rGO electrodes during the charge/discharge process in PIBs. (a) *In*/*ex situ* Raman analysis of $MoSe_{2+x}$-rGO at the 2nd cycle. (b) Raman spectra of pristine $MoSe_2$-rGO and $MoSe_2$-rGO discharged to 0.75 V and 0.5 V. (c) Raman spectra of pristine $MoSe_{2+x}$-rGO and $MoSe_{2+x}$-rGO discharged to 1.0 V and 0.5 V. (d) Energy difference (Δ*E*) of excess selenium at different positions. Charge/discharge profiles with schematic diagrams of the reaction mechanism of (e) $MoSe_2$-rGO and (f) $MoSe_{2+0.2}$-rGO (take $x = 0.2$ as an example for $MoSe_{2+x}$-rGO).

To gain insight into the structural and compositional evolution of the $MoSe_{2+x}$-rGO electrode, *in*/*ex situ* Raman spectroscopy during the second cycle was carried out. As illustrated in Fig. 4a, a distinct peak appeared at 252 cm^{-1} when discharged approximately to 0.64 V, which corresponded to the characteristic peak of K_2Se.[24] The generation of K_2Se indicated that the system underwent a conversion reaction, and the final discharge products included K_2Se. When charged approximately to 1.0 V, the characteristic peak of K_2Se disappeared. To get a clearer picture of the mechanism, we selected some representative Raman spectra of $MoSe_{2+x}$-rGO and $MoSe_2$-rGO discharged to specific potentials. The Raman spectra of $MoSe_2$-rGO at specific potentials are displayed in Fig. 4b. When $MoSe_2$-rGO was discharged to 0.5 V, only the intercalation reaction occurred, which was consistent with previous reports on the reaction mechanism of $MoSe_2$-based electrodes.[15,18] As shown in Fig. 4c, when $MoSe_{2+x}$-rGO was discharged to 1.0 V, the shift of A_{1g} and E^1_{2g} peaks to higher angles was attributed to the intercalation of K^+ into $MoSe_{2+x}$, while there was no peak of K_2Se observed at this time. When discharged to 0.5 V, the characteristic peak of K_2Se appeared, which was owing to the conversion reaction offered by the Se atoms in the interlayer. The above results indicated that the $MoSe_{2+x}$-rGO system underwent an intercalation reaction firstly, followed by a conversion reaction. The intercalation reaction is generally known to display excellent cycling stability but low discharge capacity and slow ion diffusion rate.[55,56] In contrast, high capacity can be achieved in conversion reactions. However, conversion reactions usually suffer from the shuttle effect, which leads to a rapid decay of capacity.[57] Bond modulation, which drives a dual reaction mechanism in which the intercalation and conversion reactions complement each other, is an effective method to improve the capacity and reversibility of the $MoSe_{2+x}$-rGO cathode. To summarize, one of the reasons why $MoSe_{2+x}$-rGO has a much higher capacity than $MoSe_2$-rGO is that $MoSe_{2+x}$-rGO not only undergoes an intercalation reaction but also a conversion reaction, which offers extra capacity. Moreover, when charged to 3.0 V, the Raman spectrum of $MoSe_{2+x}$-rGO was identical to that of the pristine state, which demonstrated the high reversibility of the reaction (Fig. S14†). Since HRTEM images could not identify the exact position of the excess Se atoms between $MoSe_2$ layers, we determined the position of the interlayer Se atoms by density functional theory (DFT) calculations (Fig. 4d). We selected three positions: the Mo–Se bond bridge, the center of the hexagon, and the top of the Mo atom. It was found that the lowest energy, *i.e.* the most stable position, was possessed at the Mo–Se bond bridge position. In addition, DFT calculations indicated that both $MoSe_{2+x}$-rGO and $MoSe_2$-rGO underwent the intercalation reaction, but the amount of inserted potassium was quite different due to bond modulation. $MoSe_2$-rGO could only be intercalated with one-third of K^+, while $MoSe_{2+x}$-rGO could be intercalated with two-thirds of K^+ (Fig. 4e and f). This is the other reason why the capacity of $MoSe_{2+x}$-rGO was much higher than that of $MoSe_2$-rGO. We roughly estimated that the capacity contributions of the intercalation reaction and conversion reaction of $MoSe_{2+0.2}$-rGO are 58.1% and 41.9% at 100 mA g^{-1}, respectively. In addition, the capacity contribution may vary at different current densities because of the distinct kinetics, which has been reported previously.[58]

We believed the excellent rate performance of the $MoSe_{2+x}$-rGO cathode significantly depended on the kinetics origin, which was investigated by CV tests in detail. The CV profiles of $MoSe_{2+x}$-rGO and $MoSe_2$-rGO at different scan rates are shown in Fig. S15a and S16a.† The surface-controlled capacitive process (k_1v_1) and diffusion-controlled intercalation process (k_2v_2) together determine the capacity contribution of an electrode according to the following equation:

$$i = k_1 v_1 + k_2 v^{\frac{1}{2}}$$

where i and v are the current and scan rate, respectively. Generally, through the power law $i = av^b$, the relationship between the current (i) and scan rate (v) can be evaluated. When the b value is close to 0.5, the diffusion-controlled process is predominant, for example when the b values of $MoSe_{2+x}$-rGO were 0.88 and 0.85 and the b value of $MoSe_2$-rGO was 0.77, which indicated that pseudocapacitance played a major role in both $MoSe_{2+x}$-rGO and $MoSe_2$-rGO electrodes. Fig. S15c and S16c† exhibit the corresponding pseudocapacitance contributions of $MoSe_{2+x}$-rGO and $MoSe_2$-rGO at different scan rates. The $MoSe_{2+x}$-rGO displayed an obviously larger pseudocapacitance contribution (56.6–83.5%) than $MoSe_2$-rGO (49.9–78.8%) at the scan rate range from 0.1 to 1.5 mV s^{-1}, resulting in a better rate performance (Fig. S15d and S16d†). Moreover, the galvanostatic intermittent titration technique (GITT) was used to evaluate the diffusion coefficient of K^+ in an electrode based on the equation:

$$D = \frac{4}{\pi\tau}\left(\frac{L}{S}\right)^2\left(\frac{\Delta E_s}{\Delta E_t}\right)^2$$

where τ is the relaxation time (s); t is the duration of the applied current pulse; L is the diffusion length of K^+ (for compact electrodes, the value of L equals the thickness of the electrode); ΔE_s is the voltage change caused by the pulse current; and ΔE_t is the voltage change during charging and discharging at a constant current. Fig. S17a† shows the GITT curves of $MoSe_{2+x}$-rGO and $MoSe_2$-rGO during the discharge/charge process, and the corresponding K^+ diffusion coefficient (D_{K^+}) at different insertion/extraction states is displayed in Fig. S17b.† The average D_{K^+} of $MoSe_{2+x}$-rGO was about 2.7×10^{-10} and 3.86×10^{-10} cm^2 s^{-1} during the potassiation/depotassiation process, respectively. However, the average D_{K^+} of $MoSe_2$-rGO was about 1.32×10^{-10} cm^2 s^{-1} during the discharge process and 3.04×10^{-10} cm^2 s^{-1} during the charging process, which were smaller than that of $MoSe_{2+x}$-rGO, demonstrating the faster diffusion of K^+ in $MoSe_{2+x}$-rGO than $MoSe_2$-rGO.

Electrochemical impedance spectroscopy measurements (Fig. S18,† the inset picture is the equivalent circuit) were carried out. R_{ct} is the charge-transfer resistance at interfaces and Z_w is the Warburg impedance corresponding to K^+ diffusion in the equivalent circuit. After fitting, the R_{ct} value of $MoSe_{2+x}$-rGO increased slightly as the number of cycles increased, which was due to the formation of a more stable SEI during cycling. Meanwhile, the slope of the straight line became larger during cycling, suggesting an enhancement of the K^+ diffusion ability.[59] It was obvious that the R_{ct} of $MoSe_{2+x}$-rGO was much lower than that of $MoSe_2$-rGO and pure $MoSe_{2+x}$ at the 50th and 100th cycles, demonstrating the superior kinetics of $MoSe_{2+x}$-rGO due to its high electrical and ionic conductivity at the heterointerface.[55] The SEM images of the pristine $MoSe_{2+x}$-rGO and $MoSe_2$-rGO electrodes and those after cycling are shown in Fig. S19 and S20.† The structure of the $MoSe_{2+x}$-rGO electrode remained almost unchanged, while a certain degree of structural failure occurred in the $MoSe_2$-rGO electrode. The structural collapse may be a major factor for the poor electrochemical kinetics of the $MoSe_2$-rGO electrode.[60] In contrast, $MoSe_{2+x}$-rGO could maintain the integrity of the structure. The XRD spectrum of $MoSe_{2+x}$-rGO after cycling showed that no obvious peak appeared other than for aluminum (Fig. S21†). The HRTEM of $MoSe_{2+x}$-rGO was performed after cycling (Fig. S22†). After 50 cycles, no more layered crystals were found and the materials changed to amorphous particles with low contrast.[58,61]

Furthermore, we explored the cycling performance of potassium-ion full cells (PIFCs) in which $MoSe_{2+x}$-rGO was used as the cathode and Nano Graphite (NG) was adopted as the anode. The capacity and current density of the PIFC were calculated based on the mass of the $MoSe_{2+x}$-rGO cathode. The normalized discharge/charge curves of the $MoSe_{2+x}$-rGO and NG electrodes in the half cell and full cell are shown in Fig. 5a. The electrochemical performance of the $MoSe_{2+x}$-rGO‖NG PIFC was examined at a current density of 100 mA g^{-1} within the voltage

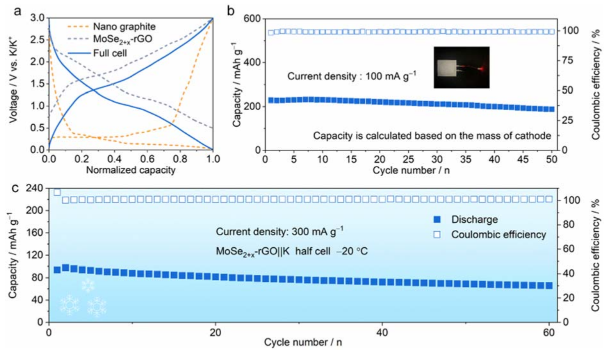

Fig. 5 Electrochemical performance of the $MoSe_{2+x}$-rGO‖NG full cell and $MoSe_{2+x}$-rGO‖K half cell at low temperature. (a) Discharge/charge profiles of the half cell and the full cell. (b) Cycling performance of the $MoSe_{2+x}$-rGO‖NG full cell at 100 mA g^{-1}; the inset is a corresponding optical image showing it powering a LED. (c) Cycling performance of the $MoSe_{2+x}$-rGO‖K half cell at 300 mA g^{-1} and −20 °C.

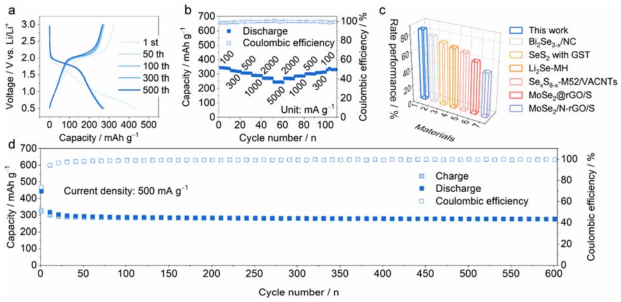

Fig. 6 Electrochemical performance of the $MoSe_{2+x}$-rGO‖K half cell for lithium-ion storage. (a) Discharge/charge curves of $MoSe_{2+x}$-rGO at different cycles. (b) Rate performance of $MoSe_{2+x}$-rGO at various current densities. (c) Comparison of the rate performance of $MoSe_{2+x}$-rGO with that of other Se-based composites for LIBs. (d) Cycling performance of $MoSe_{2+x}$-rGO at 500 mA g^{-1}.

window of 0.01–3 V after pre-cycling (Fig. 5b and S23†).[62,63] The discharge capacity of $MoSe_{2+x}$-rGO‖NG could be maintained at 81.9% of the initial capacity (188.7 mA h g^{-1}) after 50 cycles. An appreciable energy density of 246 W h kg^{-1} was achieved and it was sufficient for its application in potassium-ion battery cathode materials. Notably, the full cell delivered considerable energy density compared to other K cathode materials although its discharge voltage plateau was not very high.[20,27,64] And the CE was as high as 99% during the stable cycling of the full cell. Moreover, the $MoSe_{2+x}$-rGO‖K half cell could be operated normally at temperatures as low as −20 °C (Fig. 5c).

To demonstrate the broad compatibility in energy storage systems, $MoSe_{2+x}$-rGO was also investigated as the cathode for LIBs. As shown in Fig. 6a and S24,† the highly overlapped charge/discharge and CV curves showed low polarization and high electrochemical reversibility of $MoSe_{2+x}$-rGO in the LIB system. The cycling performance of $MoSe_{2+x}$-rGO for LIBs at a current density of 500 mA g^{-1} is shown in Fig. 6d, exhibiting a high capacity and considerable capacity retention (maintaining 267 mA h g^{-1} after 600 cycles), and the CE was above 99.5% on average. Fig. 6b shows an impressive rate performance of 334, 316, 304, 288, 271 and 245 mA h g^{-1} at current densities of 100, 300, 500, 1000, 2000 and 5000 mA g^{-1}, respectively. The corresponding charge/discharge profiles at various current densities are shown in Fig. S25.† The rate performance of Se-based cathodes in LIBs in recent years was compared with this work (Fig. 6c and Table S2†). Clearly, the $MoSe_{2+x}$-rGO cathode demonstrated the best rate performance among them.

Conclusions

In summary, Se atoms were introduced to randomly spread between $MoSe_2$ layers by means of bond modulation, and the introduced Se atoms formed covalent Se–Se bonds with the Se atoms in $MoSe_2$. The approach of bond modulation gives the $MoSe_{2+x}$-rGO cathode many advantages, including: (1) enlarging the interlayer spacing along the [002] axis, which allows easier and more insertion of K^+; (2) achieving a dual reaction mechanism, with additional conversion reaction providing more capacity for $MoSe_{2+x}$-rGO; and (3) confining the introduced Se atoms in the interlayer to avoid the shuttle effect. Thanks to the above advantages, $MoSe_{2+x}$-rGO exhibited an impressive K^+ storage ability, including an ultrahigh capacity with a long cycle life (300 cycles at 100 mA g^{-1}) and a superior rate capability (89 mA h g^{-1} retained at a high current density of 2000 mA g^{-1}). Notably, the full cell delivered a considerable energy density compared to other K cathode materials although its discharge voltage plateau was not very high. The $MoSe_{2+x}$-rGO cathode also displayed an extraordinary cycling stability (retaining 267 mA h g^{-1} at 500 mA g^{-1} over 600 cycles) and a desirable rate performance (245 mA h g^{-1} at 5000 mA g^{-1}) for LIBs. The strategy of bond modulation inducing combined intercalation and conversion reactions provides a new opportunity to achieve high capacity and long cycle life K cathodes.

Data availability

All data needed to evaluate the conclusions in the paper are present in the paper and/or the ESI.† And all data can be obtained from the authors.

Author contributions

The manuscript was written through contributions of all authors. All authors have given approval to the final version of the manuscript.

Conflicts of interest

The authors declare no conflict of interest.

Acknowledgements

This work was financially supported by the National Natural Science Foundation of China (No. U20A20247 and 51922038).

Notes and references

1 M. Chhowalla, H. S. Shin, G. Eda, L. J. Li, K. P. Loh and H. Zhang, The chemistry of two-dimensional layered transition metal dichalcogenide nanosheets, *Nat. Chem.*, 2013, **5**, 263–275.
2 B. Chen, T. S. Wang, S. Y. Zhao, J. Y. Tan, N. Q. Zhao, S. P. Jiang, Q. F. Zhang, G. M. Zhou and H. M. Cheng, Efficient Reversible Conversion between MoS_2 and Mo/Na_2S Enabled by Graphene-Supported Single Atom Catalysts, *Adv. Mater.*, 2021, **33**, 2007090.
3 X. Zhang, Z. Lai, Q. Ma and H. Zhang, Novel structured transition metal dichalcogenide nanosheets, *Chem. Soc. Rev.*, 2018, **47**, 3301–3338.
4 X. Li and J. Wang, One-dimensional and two-dimensional synergized nanostructures for high-performing energy storage and conversion, *InfoMat*, 2020, **2**, 3–32.

5 X. Tong, K. Liu, M. Zeng and L. Fu, Vapor-phase growth of high-quality wafer-scale two-dimensional materials, *InfoMat*, 2019, **1**, 460–478.

6 Y. Li, M. Wang and J. Sun, Molecular Engineering Strategies toward Molybdenum Diselenide Design for Energy Storage and Conversion, *Adv. Energy Mater.*, 2022, **n/a**, 2202600.

7 C. P. Yang, Y. X. Yin and Y. G. Guo, Elemental Selenium for Electrochemical Energy Storage, *J. Phys. Chem. Lett.*, 2015, **6**, 256–266.

8 P. L. He, Y. J. Fang, X. Y. Yu and X. W. Lou, Hierarchical Nanotubes Constructed by Carbon-Coated Ultrathin SnS Nanosheets for Fast Capacitive Sodium Storage, *Angew. Chem., Int. Ed.*, 2017, **56**, 12202–12205.

9 J. Chen, A. Pan, Y. Wang, X. Cao, W. Zhang, X. Kong, Q. Su, J. Lin, G. Cao and S. Liang, Hierarchical mesoporous $MoSe_2$@CoSe/N-doped carbon nanocomposite for sodium ion batteries and hydrogen evolution reaction applications, *Energy Storage Mater.*, 2019, **21**, 97–106.

10 W. Wang, B. Jiang, C. Qian, F. Lv, J. Feng, J. Zhou, K. Wang, C. Yang, Y. Yang and S. Guo, Pistachio-Shuck-Like $MoSe_2$/C Core/Shell Nanostructures for High-Performance Potassium-Ion Storage, *Adv. Mater.*, 2018, **30**, 1801812.

11 X. Hu, W. Zhang, X. Liu, Y. Mei and Y. Huang, Nanostructured Mo-based electrode materials for electrochemical energy storage, *Chem. Soc. Rev.*, 2015, **44**, 2376–2404.

12 A. Eftekhari, Molybdenum diselenide ($MoSe_2$) for energy storage, catalysis, and optoelectronics, *Appl. Mater. Today*, 2017, **8**, 1–17.

13 F. Niu, J. Yang, N. Wang, D. Zhang, W. Fan, J. Yang and Y. Qian, $MoSe_2$-Covered N,P-Doped Carbon Nanosheets as a Long-Life and High-Rate Anode Material for Sodium-Ion Batteries, *Adv. Funct. Mater.*, 2017, **27**, 1700522.

14 P. Ge, H. Hou, C. E. Banks, C. W. Foster, S. Li, Y. Zhang, J. He, C. Zhang and X. Ji, Binding $MoSe_2$ with carbon constrained in carbonous nanosphere towards high-capacity and ultrafast Li/Na-ion storage, *Energy Storage Mater.*, 2018, **12**, 310–323.

15 Y. Yi, Z. Sun, C. Li, Z. Tian, C. Lu, Y. Shao, J. Li, J. Sun and Z. Liu, Designing 3D Biomorphic Nitrogen-Doped $MoSe_2$/Graphene Composites toward High-Performance Potassium-Ion Capacitors, *Adv. Funct. Mater.*, 2020, **30**, 1903878.

16 R. Zhou, H. Wang, J. Chang, C. Yu, H. Dai, Q. Chen, J. Zhou, H. Yu, G. Sun and W. Huang, Ammonium Intercalation Induced Expanded 1T-Rich Molybdenum Diselenides for Improved Lithium Ion Storage, *ACS Appl. Mater. Interfaces*, 2021, **13**, 17459–17466.

17 Z. Shi, Z. Sun, J. Cai, X. Yang, C. Wei, M. Wang, Y. Ding and J. Sun, Manipulating Electrocatalytic Li_2S Redox via Selective Dual-Defect Engineering for Li–S Batteries, *Adv. Mater.*, 2021, **33**, 2103050.

18 M. Ma, S. Zhang, Y. Yao, H. Wang, H. Huang, R. Xu, J. Wang, X. Zhou, W. Yang, Z. Peng, X. Wu, Y. Hou and Y. Yu, Heterostructures of 2D Molybdenum Dichalcogenide on 2D Nitrogen-Doped Carbon: Superior Potassium-Ion Storage and Insight into Potassium Storage Mechanism, *Adv. Mater.*, 2020, **32**, 2000958.

19 J. Sheng, T. Wang, J. Tan, W. Lv, L. Qiu, Q. Zhang, G. Zhou and H.-M. Cheng, Intercalation-Induced Conversion Reactions Give High-Capacity Potassium Storage, *ACS Nano*, 2020, **14**, 14026–14035.

20 T. Hosaka, K. Kubota, A. S. Hameed and S. Komaba, Research Development on K-Ion Batteries, *Chem. Rev.*, 2020, **120**, 6358–6466.

21 H. Kong, Y. Guan, J. Wang, W. Sun, L. Chen, J. Ou, L. Xie, F. Fu, H. Zhang and H. Chen, An intercalation–conversion hybrid mechanism enables covalent organic frameworks with superior Li-ion storage, *J. Mater. Chem. A*, 2022, **10**, 20866–20873.

22 S. Liu, L. Kang and S. C. Jun, Challenges and Strategies toward Cathode Materials for Rechargeable Potassium-Ion Batteries, *Adv. Mater.*, 2021, **33**, 2004689.

23 J. Sun, H. W. Lee, M. Pasta, H. Yuan, G. Y. Zheng, Y. M. Sun, Y. Z. Li and Y. Cui, A phosphorene–graphene hybrid material as a high-capacity anode for sodium-ion batteries, *Nat. Nanotechnol.*, 2015, **10**, 980–985.

24 R. Xu, Y. Yao, H. Y. Wang, Y. F. Yuan, J. W. Wang, H. Yang, Y. Jiang, P. C. Shi, X. J. Wu, Z. Q. Peng, Z. S. Wu, J. Lu and Y. Yu, Unraveling the Nature of Excellent Potassium Storage in Small-Molecule Se@Peapod-Like N-Doped Carbon Nanofibers, *Adv. Mater.*, 2020, **32**, 2003879.

25 G. Zhou, H. Chen and Y. Cui, Formulating energy density for designing practical lithium–sulfur batteries, *Nat. Energy*, 2022, **7**, 312–319.

26 J. Heo, S. K. Jung, I. Hwang, S. P. Cho, D. Eum, H. Park, J. H. Song, S. Yu, K. Oh, G. Kwon, T. Hwang, K. H. Ko and K. Kang, Amorphous iron fluorosulfate as a high-capacity cathode utilizing combined intercalation and conversion reactions with unexpectedly high reversibility, *Nat. Energy*, 2023, **8**, 30–39.

27 C. Zhang, Y. Xu, M. Zhou, L. Liang, H. Dong, M. Wu, Y. Yang and Y. Lei, Potassium Prussian Blue Nanoparticles: A Low-Cost Cathode Material for Potassium-Ion Batteries, *Adv. Funct. Mater.*, 2017, **27**, 1604307.

28 C. Yu, Z. F. Cao, S. Chen, S. Wang and H. Zhong, Promoting the hydrogen evolution performance of 1T-$MoSe_2$-Se: Optimizing the two-dimensional structure of $MoSe_2$ by layered double hydroxide limited growth, *Appl. Surf. Sci.*, 2020, **509**, 145364.

29 J. Wang, Q. Zhang, J. Sheng, Z. Liang, J. Ma, Y. Chen, G. Zhou and H.-M. Cheng, Direct and green repairing of degraded $LiCoO_2$ for reuse in lithium-ion batteries, *Natl. Sci. Rev.*, 2022, **9**, nwac097.

30 S. Chong, X. Wei, Y. Wu, L. Sun, C. Shu, Q. Lu, Y. Hu, G. Cao and W. Huang, Expanded $MoSe_2$ Nanosheets Vertically Bonded on Reduced Graphene Oxide for Sodium and Potassium-Ion Storage, *ACS Appl. Mater. Interfaces*, 2021, **13**, 13158–13169.

31 H. Liu, B. Liu, H. Guo, M. Liang, Y. Zhang, T. Borjigin, X. Yang, L. Wang and X. Sun, N-doped C-encapsulated scale-like yolk-shell frame assembled by expanded planes

few-layer $MoSe_2$ for enhanced performance in sodium-ion batteries, *Nano Energy*, 2018, **51**, 639–648.

32 H. Matte, A. Gomathi, A. K. Manna, D. J. Late, R. Datta, S. K. Pati and C. N. R. Rao, MoS_2 and WS_2 Analogues of Graphene, *Angew. Chem., Int. Ed.*, 2010, **49**, 4059–4062.

33 H. Peng, C. Wei, K. Wang, T. Meng, G. Ma, Z. Lei and X. Gong, $Ni_{0.85}Se@MoSe_2$ Nanosheet Arrays as the Electrode for High-Performance Supercapacitors, *ACS Appl. Mater. Interfaces*, 2017, **9**, 17067–17075.

34 F. Sun, H. Cheng, J. Chen, N. Zheng, Y. Li and J. Shi, Heteroatomic $SenS_8$–n Molecules Confined in Nitrogen-Doped Mesoporous Carbons as Reversible Cathode Materials for High-Performance Lithium Batteries, *ACS Nano*, 2016, **10**, 8289–8298.

35 X. Wang, Y. Tan, Z. Liu, Y. Fan, M. Li, H. A. Younus, J. Duan, H. Deng and S. Zhang, New Insight into the Confinement Effect of Microporous Carbon in Li/Se Battery Chemistry: A Cathode with Enhanced Conductivity, *Small*, 2020, **16**, 2000266.

36 Z. Luo, J. Zhou, L. Wang, G. Fang, A. Pan and S. Liang, Two-dimensional hybrid nanosheets of few layered $MoSe_2$ on reduced graphene oxide as anodes for long-cycle-life lithium-ion batteries, *J. Mater. Chem. A*, 2016, **4**, 15302–15308.

37 L. Zeng, X. Chen, R. Liu, L. Lin, C. Zheng, L. Xu, F. Luo, Q. Qian, Q. Chen and M. Wei, Green synthesis of a Se/HPCF–rGO composite for Li–Se batteries with excellent long-term cycling performance, *J. Mater. Chem. A*, 2017, **5**, 22997–23005.

38 M. Liu, P. Zhang, Z. Qu, Y. Yan, C. Lai, T. Liu and S. Zhang, Conductive carbon nanofiber interpenetrated graphene architecture for ultra-stable sodium ion battery, *Nat. Commun.*, 2019, **10**, 3917.

39 H. Kim, D.-H. Seo, M. Bianchini, R. J. Clément, H. Kim, J. C. Kim, Y. Tian, T. Shi, W. S. Yoon and G. Ceder, A New Strategy for High-Voltage Cathodes for K-Ion Batteries: Stoichiometric $KVPO_4F$, *Adv. Energy Mater.*, 2018, **8**, 1801591.

40 J. Y. Hwang, J. Kim, T. Y. Yu, H. G. Jung, J. Kim, K. H. Kim and Y. K. Sun, A new P2-type layered oxide cathode with superior full-cell performances for K-ion batteries, *J. Mater. Chem. A*, 2019, **7**, 21362–21370.

41 J. Liao, Q. Hu, J. Mu, X. He, S. Wang and C. Chen, A vanadium-based metal–organic phosphate framework material $K_2[(VO)_2(HPO_4)_2(C_2O_4)]$ as a cathode for potassium-ion batteries, *Chem. Commun.*, 2019, **55**, 659–662.

42 X. Lin, J. Huang, H. Tan, J. Huang and B. Zhang, $K_3V_2(PO_4)_2F_3$ as a robust cathode for potassium-ion batteries, *Energy Storage Mater.*, 2019, **16**, 97–101.

43 Q. Xue, L. Li, Y. Huang, R. Huang, F. Wu and R. Chen, Polypyrrole-Modified Prussian Blue Cathode Material for Potassium Ion Batteries via In Situ Polymerization Coating, *ACS Appl. Mater. Interfaces*, 2019, **11**, 22339–22345.

44 J. U. Choi, Y. Ji Park, J. H. Jo, Y. H. Jung, D. C. Ahn, T. Y. Jeon, K. S. Lee, H. Kim, S. Lee, J. Kim and S. T. Myung, An optimized approach toward high energy density cathode material for K-ion batteries, *Energy Storage Mater.*, 2020, **27**, 342–351.

45 S. Lv, J. Yuan, Z. Chen, P. Gao, H. Shu, X. Yang, E. Liu, S. Tan, M. Ruben, Z. Zhao-Karger and M. Fichtner, Copper Porphyrin as a Stable Cathode for High-Performance Rechargeable Potassium Organic Batteries, *ChemSusChem*, 2020, **13**, 2286–2294.

46 L. Li, Z. Hu, Y. Lu, C. C. Wang, Q. Zhang, S. Zhao, J. Peng, K. Zhang, S. L. Chou and J. Chen, A Low-Strain Potassium-Rich Prussian Blue Analogue Cathode for High Power Potassium-Ion Batteries, *Angew. Chem., Int. Ed.*, 2021, **60**, 13050–13056.

47 Z. Wang, W. Zhuo, J. Li, L. Ma, S. Tan, G. Zhang, H. Yin, W. Qin, H. Wang, L. Pan, A. Qin and W. Mai, Regulation of ferric iron vacancy for Prussian blue analogue cathode to realize high-performance potassium ion storage, *Nano Energy*, 2022, **98**, 107243.

48 Q. Shen, P. Jiang, H. He, C. Chen, Y. Liu and M. Zhang, Encapsulation of $MoSe_2$ in carbon fibers as anodes for potassium ion batteries and nonaqueous battery–supercapacitor hybrid devices, *Nanoscale*, 2019, **11**, 13511–13520.

49 L. Zeng, B. Kang, F. Luo, Y. Fang, C. Zheng, J. Liu, R. Liu, X. Li, Q. Chen, M. Wei and Q. Qian, Facile Synthesis of Ultra-Small Few-Layer Nanostructured $MoSe_2$ Embedded on N, P Co-Doped Bio-Carbon for High-Performance Half/Full Sodium-Ion and Potassium-Ion Batteries, *Chem. – Eur. J.*, 2019, **25**, 13411–13421.

50 Q. Jiang, S. Hu, L. Wang, Z. Huang, H.-J. Yang, X. Han, Y. Li, C. Lv, Y.-S. He, T. Zhou and J. Hu, Boosting potassium storage in nanosheet assembled $MoSe_2$ hollow sphere through surface decoration of MoO_2 nanoparticles, *Appl. Surf. Sci.*, 2020, **505**, 144573.

51 Q. Q. Jiang, L. Wang, Y. Wang, M. H. Qin, R. Wu, Z. X. Huang, H. J. Yang, Y. X. Li, T. F. Zhou and J. C. Hu, Rational design of $MoSe_2$ nanosheet-coated MOF-derived N-doped porous carbon polyhedron for potassium storage, *J. Colloid Interface Sci.*, 2021, **600**, 430–439.

52 Y. Wu, Q. Zhang, Y. Xu, R. Xu, L. Li, Y. Li, C. Zhang, H. Zhao, S. Wang, U. Kaiser and Y. Lei, Enhanced Potassium Storage Capability of Two-Dimensional Transition-Metal Chalcogenides Enabled by a Collective Strategy, *ACS Appl. Mater. Interfaces*, 2021, **13**, 18838–18848.

53 J. Tao, Z. Yan, D. Wang, W. Zhong, Y. Yang, J. Li, Y. Lin and Z. Huang, Rational designing of $MoSe_2$ nanosheets in carbon framework for high-performance potassium-ion batteries, *Chem. Eng. J.*, 2022, **448**, 137658.

54 J. Yang, L. Liu, D. Wang, J. Tao, Y. Yang, J. Li, Y. Lin and Z. Huang, Boosting K-ion kinetics by interfacial polarization induced by amorphous MoO_{3-x} for $MoSe_2/MoO_{3-x}@rGO$ composites, *J. Mater. Sci. Technol.*, 2022, **115**, 232–240.

55 L. Wu, H. Fu, S. Li, J. Zhu, J. Zhou, A. M. Rao, L. Cha, K. Guo, S. Wen and B. Lu, Phase-engineered cathode for super-stable potassium storage, *Nat. Commun.*, 2023, **14**, 644.

56 J. Hao, H. Xia, A. M. Rao, Y. He, J. Zhou and B. Lu, All-surface-state potassium storage enabled ultra-stable potassium cathode, *Energy Storage Mater.*, 2022, **53**, 148–155.

57 X. Huang, J. Sun, L. Wang, X. Tong, S. Dou and Z. Wang, Advanced High-Performance Potassium-Chalcogen (S, Se, Te) Batteries, *Small*, 2021, **17**, 2004369.

58 X. Du, J. Huang, X. Guo, X. Lin, J.-Q. Huang, H. Tan, Y. Zhu and B. Zhang, Preserved Layered Structure Enables Stable Cyclic Performance of MoS_2 upon Potassium Insertion, *Chem. Mater.*, 2019, **31**, 8801–8809.

59 J. Ge, L. Fan, J. Wang, Q. Zhang, Z. Liu, E. Zhang, Q. Liu, X. Yu and B. Lu, $MoSe_2$/N-Doped Carbon as Anodes for Potassium-Ion Batteries, *Adv. Energy Mater.*, 2018, **8**, 1801477.

60 M. Ma, S. Zhang, L. Wang, Y. Yao, R. Shao, L. Shen, L. Yu, J. Dai, Y. Jiang, X. Cheng, Y. Wu, X. Wu, X. Yao, Q. Zhang and Y. Yu, Harnessing the Volume Expansion of MoS_3 Anode by Structure Engineering to Achieve High Performance Beyond Lithium-Based Rechargeable Batteries, *Adv. Mater.*, 2021, **33**, 2106232.

61 X. Du, X. Guo, J. Huang, Z. Lu, H. Tan, J.-Q. Huang, Y. Zhu and B. Zhang, Exploring the structure evolution of MoS_2 upon Li/Na/K ion insertion and the origin of the unusual stability in potassium ion batteries, *Nanoscale Horiz.*, 2020, **5**, 1618–1627.

62 L. Fan, H. Xie, Y. Hu, Z. Caixiang, A. M. Rao, J. Zhou and B. Lu, A tailored electrolyte for safe and durable potassium ion batteries, *Energy Environ. Sci.*, 2023, **16**, 305–315.

63 D. Shen, A. M. Rao, J. Zhou and B. Lu, High-Potential Cathodes with Nitrogen Active Centres for Quasi-Solid Proton-Ion Batteries, *Angew. Chem., Int. Ed.*, 2022, **61**, e202201972.

64 Z. Caixiang, J. Hao, J. Zhou, X. Yu and B. Lu, Interlayer-Engineering and Surface-Substituting Manganese-Based Self-Evolution for High-Performance Potassium Cathode, *Adv. Energy Mater.*, 2022, **n/a**, 2203126.